Research Article

Configurations of V^{4+} centers in the MoVO catalyst material. A systematic stability analysis of DFT results

Torstein Fjermestad[1,2] · Wen-Qing Li[1] · Alexander Genest[1,3] · Notker Rösch[4]

Received: 13 August 2020 / Accepted: 13 October 2020 / Published online: 28 October 2020

Abstract
The reactivity of a catalyst is in part determined by its geometric and electronic structure. Here we present a model that is able to describe the energy trend of the important oxidation catalyst material MoVO, as obtained from hybrid density functional calculations for various V^{4+}/V^{5+} configurations. For an exemplary V/Mo occupancy, we systematically examined the universe of all V^{4+} distributions. The distribution of these V^{4+} centers, in combination with the induced lattice distortions, plays a key role in determining the stability of the material, entailing energy variations of up to ~140 kJ mol^{-1} per unit cell. Hence, for this kind of catalyst, it is crucial to account for the V^{4+} distributions. To this end, we are proposing novel predictive models based on features like the number of Mo centers with two reduced neighbors V^{4+} and the locations of potentially reducible centers V^{5+}. For the V/Mo occupancy chosen, these models are able to describe the energy variation due to the V^{4+} distribution with root mean square errors as low as 6 kJ mol^{-1}. Accordingly, catalytically selective sites featuring pentameric units with a single polaron center are among the most of stable configurations. Another aspect of this work is to understand energy contributions of polaron arrangements bracketing Mo centers.

Keywords Mixed metal oxide MoVO · Distribution of V^{4+}/V^{5+} · V^{4+}/V^{5+} redox processes · Linear energy models · Hybrid DFT calculations

1 Introduction

In modern chemical industry, acrylic acid and acrylonitrile are important functionalized raw chemicals for producing higher-value products [1, 2]. Alkanes, in view of their better availability, are desirable raw materials for synthesizing these chemicals via selective partial oxidation or ammoxidation [1]. MoVO–type mixed metal oxides (e.g., MoVNbTe oxides) are a class of catalysts potentially useful for these types of conversions [3]. MoVNbTeO catalysts show a promising activity, yet any optimization based on insight is very challenging due to the complicated structure of these materials [4]. In 2003, an alternative MoVO catalyst material was synthesized, featuring qualitatively the same framework structure as MoVNbTeO, yet a simpler composition. This less complex material MoVO has a lower selectivity for acrylic acid when propane is used as starting

Torstein Fjermestad and Wen-Qing Li contributed equally to this work.

Electronic supplementary material The online version of this article (https://doi.org/10.1007/s42452-020-03686-y) contains supplementary material, which is available to authorized users.

✉ Alexander Genest, alexander.genest@tuwien.ac.at | [1]Institute of High Performance Computing, Agency for Science, Technology and Research, 1 Fusionopolis Way, #16-6 Connexis, Singapore 138632, Singapore. [2]Present Address: Laboratory of Catalysis and Catalytic Processes, Dipartimento di Energia, Politecnico di Milano, Laboratory of Catalysis and Catalytic Processes, via La Masa 34, 20156 Milano, Italy. [3]Institute of Materials Chemistry, Technische Universität Wien, Getreidemarkt 9, 1060 Vienna, Austria. [4]Department Chemie and Catalysis Research Center, Technische Universität München, 85747 Garching, Germany.

material, but it works better than its four-component congener when acrolein is provided [1, 5, 6].

The M1 (orthorhombic) phase of both materials, MoVO [7] and MoVNbTeO [8, 9], is the main active structure. In MoVO, compared to MoVNbTeO, the TeO species are removed from the channels and the Nb centers of the pentagonal units are replaced by Mo centers. Mechanistic insight at the atomic level [10, 11] into oxidative transformations over the M1 phase is highly desirable for understanding this type of catalysts. Specifically, the MoVO material gives rise to essentially the same processes [1, 6]. Thus, in the present work we interpreted it as model of the more complicated MoVNbTeO material.

The distribution of Mo/V at various metal sites [12–17] of the lattice and the location of V^{4+}/V^{5+} centers pose a tough challenge to modeling even the simpler material MoVO [11, 18]. The metal sites exhibit mixed occupancies by Mo and V [7, 11], which seem to vary with the synthesis approach [2, 7, 19]. A variation in Mo/V was revealed by scanning transmission electron microscopy using high-angle annular dark-field imaging [11]. V^{4+}, V^{5+}, and Mo^{6+} are the prevalent oxidation states of the metal centers in MoVO [7, 11, 20]. Certain V centers of this selective oxidation catalyst undergo V^{4+}/V^{5+} redox processes [18, 21, 22]. A detailed computational study unravelling the consequences of the distribution of V^{4+}/V^{5+} sites seems timely for a better understanding of the MoVO-type catalyst [17, 23, 24].

Atomistic models with integer Mo and V occupations of all sites are required for carrying out calculations based on density functional theory (DFT). As several sites of the catalyst material under study feature mixed occupancies, one quickly ends up with unmanageable numbers of configurations. Each of those compositions may have several dozens to even hundreds of distributions of reduced centers, V^{4+}, i.e., configurations of (small) polaron [23], that are typical for such a transition metal oxide [25, 26], have to be screened. Thus, from the very beginning, any modeling of the MoVO material is confronted with a rather large number of configurations [14]. Establishing guiding principles for screening such a large universe of configurations seems very desirable. We will alternatively use the term "polaron configuration" to indicate a certain distribution of V^{4+} centers. To this end, DFT calculations recently were carried out on a set of 14 small-polaron distributions of an explicit V configuration. The results of this small sample were subsequently used to derive a simple model for predicting the energy variation of the V^{4+}/V^{5+} distributions [23]. We were able to rationalize how the computed total energy depends on the distribution of polarons over the various V centers. In this way, we identified parameters that affect the energies of the polaron configuration. Accordingly, the stability of the material decreases with (1) the type of the site [23] that is reduced, in the order **1**(V) < **3**(V) < **7**(V) (for the site labels, see Fig. 1); (2) an increasing number of Mo centers immediately bracketed between two V^{4+} centers [23]; (3) a decreasing number of pentameric units with a single V^{4+} center [23].

This initial model was relatively successful in describing the energy trend for a small set of configurations. The current work aims at probing and generalizing this previous model as accurate hybrid DFT calculations are now available for 60 symmetry-inequivalent structures, that may be extrapolated to all 210 polaron configurations associated, with the chosen V/Mo distribution. By exploring the origin of the model parameters, we set out to determine an improved model that may also be applied to alternative occupancies. The central aim of the present study is to understand, for a given occupancy of V and Mo, the energetics of all polaron distributions with the help of linear regression models such that general aspects of other occupancies and even other oxides may be gleaned.

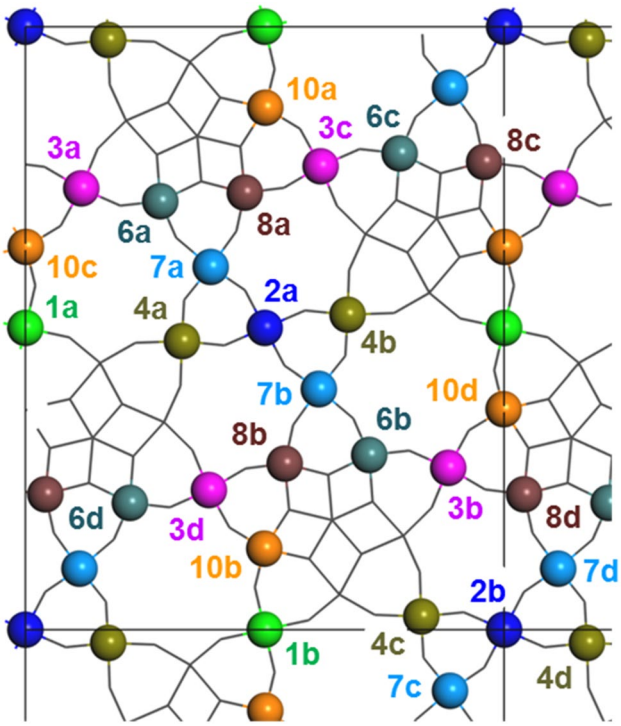

Fig. 1 Sketch of the atomic structure of the unit cell $Mo_{30}V_{10}O_{112}$ (top view). Vanadium at the sites **1**, **3** and **7**; molybdenum at the sites **2**, **4**, **6**, **8**, and **10**. Atoms equivalent in the space group Pba2 are discriminated by letters **a**, **b**, **c**, or **d**

2 Models and methods

2.1 Models

We started with a periodic model using the (experimental) unit cell of the orthorhombic M1 phase of the MoVO material [7]. From an elemental analysis [7], we derived the formula $Mo_{30}V_{10}O_{112}$ for the primitive unit cell, using the highest occupancies of all metal sites [7]. The ideal material shows a layered structure [23, 24] with a unit cell that belongs to the space group Pba2, Fig. 1. In this structure, one finds three types of symmetry inequivalent centers occupied by V atoms, 8 centers occupied by Mo atoms, and 29 centers by O atoms. For easy comparison, we use the same nomenclature as in our previous work [9, 23, 24]. Accordingly, the symmetry inequivalent sites occupied by Mo and V centers in the unit cell are referred to by the labels $\boldsymbol{n} = \mathbf{1}, \mathbf{2}, \ldots, \mathbf{11}$, Fig. 1. We distinguish symmetry equivalent sites by adding a letter. **a**, **b**, **c**, or **d**, to the site labels ***n***.

A primitive, neutral unit cell of the composition $Mo_{30}V_{10}O_{112}$ includes six reducing electrons under the hypothesis that all metals are fully oxidized, i.e., V^{5+} and Mo^{6+}. As indicated by XANES [18], these electrons preferentially locate at V centers, leading to the V redox couple V^{4+}/V^{5+}. Therefore, we assume these extra electrons to occupy 6 of 10 V centers, resulting in ${}_6C_{10} = 210$ distributions in total, of which 60 are symmetry inequivalent. Two, four, eight, and 46 symmetry inequivalent structures belong to the space groups Pba2, P2, Pc, and P1, respectively. Each of the two structures of the space group Pba2 is unique. Each of the four structures with space group P2 is two-fold degenerate; the same holds for each of the eight structures with space group Pc. The degenerate structures can be obtained by applying a two-fold rotation around an axis along the *c* direction or one of the two glide reflections (mirror operations followed by a suitable translation) of the full space group Pba2. Each of the 46 structures of space group P1 is associated with three other, degenerate structures; these associated structures may be generated by applying one of the non-trivial symmetry operations of the space group Pba2. We refer the reader to Sect. S1 of the Electronic Supplementary Material (ESM) for details of how we constructed the complete manifold to achieve a proper weighting of the 60 symmetry inequivalent structures.

To characterize the 60 symmetry-inequivalent structures, we use the nomenclature previously introduced [23] with labels indicating the six reduced V sites. For example, the label **1ab3abcd** represents a configuration where the V centers at sites **1a**, **1b**, **3a**, **3b**, **3c**, and **3d** are reduced, Fig. 1 and Table 1. For easier reading, we alternatively enumerate these structures by the labels **1**, …, **60**, Table 1. We carried out electronic structure calculations of the 60 symmetry-unique polaron configurations and derived the energies of the remaining 150 of the 210 configurations in total by applying suitable symmetry operations of space group Pba2; see above.

2.2 Computational method

In the electronic structure calculations, we applied a method based on Density Functional Theory (DFT) to periodic models with a single-layer unit cell. For solving the Kohn-Sham problem (in the spin-unrestricted fashion), we chose the hybrid functional B3LYP [27] as implemented in the code CRYSTAL14 [28], as evaluated favorably in our earlier benchmark studies [29, 30]. In this way, the localization of unpaired electrons at transition metal centers and the oxidation states of the latter can be well described [23]. Van der Waals interactions were approximated with the D2 method [31]. We chose the following Gaussian-type basis sets: 86-411d31G for V [32], 8-411d1 for O [33], and 5-11G* for H [34]. For Mo, we used the valence basis set [35] 311(d31)G in combination with a Hay-Wadt small-core effective core potential [36]. We converged the Kohn-Sham SCF procedure to 10^{-7} a.u. Structures were considered converged, when the RMS value for atomic displacements fell below 1.2×10^{-3} a.u. and simultaneously the RMS value for the gradients was below 3.0×10^{-4} a.u. We used a $1 \times 1 \times 4$ k-point mesh to carry out the integrations over the Brillouin zone [37]. No symmetry constraints were applied.

We restrict the discussion below to results for unpaired electrons, all aligned in parallel, on 6 V centers, to avoid methodologic complications. Applying a Mulliken population analysis to the spin density, we identified the V^{4+} centers and the corresponding localized states in the band gap, 1.5–2 eV below the bottom of the conduction band, based on their partially occupied 3*d* shell [30]. We interpreted a spin density of at least 0.9 *e* as sufficient to identify a center as reduced in the spirit of previous work [30]. The localization of V^{4+} centers was achieved by expanding the V–O bonds at the polaron center in question [30]. For further computational details, we refer to our previous work [23].

To analyze the lattice distortions caused by the small polarons, we determined an ideal structure, referred to as **Ox**, of the $Mo_{30}V_{10}O_{112}$ unit cell without any polarons, i.e., with all metal centers fully oxidized, V^{5+} or Mo^{6+}. As such, this unit cell carries a charge of +6 *e*; to keep the system neutral, we added a uniform background charge, −6 *e* [38]. In that electronic structure calculation of **Ox**, we fixed the lattice parameters at their experimental values [7] and relaxed the atomic positions within the unit cell. For all other structures we optimized both parameters.

Table 1 Configurations of the bulk structures of with six V^{4+} centers. For the sites **1**, **3**, and **7** and the locations **a**, **b**, **c**, and **d**, see Fig. 1. Energy values[a] E_{DFT} from DFT calculations and the corresponding results E_C of model C (kJ mol^{-1})

Label	V^{4+}			Energy		Label	V^{4+}			Energy	
	1(V)	**3**(V)	**7**(V)	DFT	C		**1**(V)	**3**(V)	**7**(V)	DFT	C
1[a]	**ab**	**abcd**		−9.1	−11.5	**31**	**ab**	**c**	**abd**	18.7	18.0
2	**ab**		**abcd**	38.8	46.3	**32**	**b**	**acd**	**ad**	21.0	17.4
3[a]	**ab**	**ab**	**cd**	35.8	35.3	**33**	**b**	**acd**	**bc**	24.0	17.4
4[a]	**ab**	**cd**	**cd**	39.6	35.3	**34**	**ab**	**c**	**abc**	24.5	26.9
5		**abcd**	**cd**	69.4	73.2	**35**	**ab**	**d**	**bcd**	24.9	26.9
6		**ab**	**abcd**	108.8	120.0	**36**	**b**	**acd**	**ac**	28.8	26.4
7	**ab**	**ad**	**ad**	−17.1	−10.4	**37**	**ab**	**ad**	**cd**	33.9	35.3
8	**ab**	**ac**	**bd**	−13.2	−28.3	**38**	**a**	**cd**	**acd**	37.6	45.8
9	**ab**	**ad**	**bc**	−11.5	−10.4	**39**	**ab**	**ac**	**cd**	43.5	35.3
10	**ab**	**ac**	**ac**	6.1	7.4	**40**	**a**	**cd**	**abc**	46.3	45.8
11		**abcd**	**bc**	20.9	27.4	**41**	**a**	**ad**	**acd**	48.6	54.8
12		**abcd**	**ac**	23.0	27.4	**42**	**b**	**ad**	**abc**	48.9	54.8
13		**ad**	**abcd**	107.3	120.0	**43**	**a**	**acd**	**cd**	50.3	54.2
14		**ac**	**abcd**	119.9	120.0	**44**	**b**	**ad**	**acd**	54.0	54.8
15	**ab**	**ad**	**ac**	−15.8	−10.4	**45**	**b**	**ac**	**abd**	57.3	45.8
16	**ab**	**cd**	**ac**	−15.5	−10.4	**46**	**b**	**ad**	**bcd**	59.4	54.8
17	**ab**	**cd**	**ad**	−12.9	−10.4	**47**	**a**	**acd**	**ab**	60.7	54.2
18	**ab**	**acd**	**d**	−9.1	−11.0	**48**	**b**	**cd**	**abc**	63.3	63.7
19	**ab**	**acd**	**c**	−6.4	−2.0	**49**	**b**	**acd**	**ab**	64.0	63.2
20	**ab**	**acd**	**a**	−6.3	−2.0	**50**	**b**	**ac**	**abc**	65.4	63.7
21	**ab**	**acd**	**b**	−6.3	−11.0	**51**	**b**	**ac**	**bcd**	68.5	45.8
22	**ab**	**ac**	**ad**	−1.3	−10.4	**52**	**b**	**cd**	**acd**	69.9	63.7
23	**a**	**acd**	**bd**	2.7	−0.4	**53**		**acd**	**abd**	70.1	73.7
24	**b**	**abcd**	**a**	8.4	8.0	**54**		**acd**	**bcd**	71.5	73.7
25	**a**	**acd**	**ad**	10.0	8.5	**55**	**b**	**acd**	**cd**	72.2	63.2
26	**b**	**abcd**	**c**	10.3	8.0	**56**		**acd**	**acd**	76.1	82.6
27	**a**	**acd**	**bc**	12.9	8.5	**57**		**acd**	**abc**	77.4	82.6
28	**b**	**acd**	**bd**	15.3	8.5	**58**	**b**	**b**	**abcd**	80.0	83.2
29	**a**	**acd**	**ac**	16.5	17.4	**59**	**b**	**ac**	**acd**	82.1	63.7
30	**ab**	**c**	**bcd**	18.1	18.0	**60**	**b**	**c**	**abcd**	93.3	92.1

[a]DFT energies relative to the value of a previously obtained isomer **1′** of structure **1**, Ref. [23]

2.3 Statistical methods

To associate features of the system with the set of DFT energies, one may invoke regression methods [39], as done previously [23, 24]. Thereby, one approximates the energy vector $\boldsymbol{E}_{DFT}$ of DFT results in a multiple linear regression model M of the form $\boldsymbol{E}_M = \mathbf{N}\,\boldsymbol{\varepsilon} + C_M$ where $\boldsymbol{E}_M$ is the vector of the model energies. The matrix **N** describes the features of the system, the vector $\boldsymbol{\varepsilon}$ holds the regression coefficients. The ordinate intercept C_M shifts the energy to match the reference system. The features **N** are *a priori* countable quantities, e.g., polarons shifted with respect to a reference state.

In view of the relatively large number of features desired, we resorted in the following to a partial least square regression (PLSR) method as implemented in the library Scikit-learn [40] for minimizing the length of the difference vector $\Delta\boldsymbol{E} = \boldsymbol{E}_M - \boldsymbol{E}_{DFT}$ in iterative fashion. PLSR was developed to deal with regression problems that potentially require tackling collinearity challenges [41]. The truly independent linear combinations of features will be referred to as "components", resulting from the PLSR procedure. The number of components was optimized with respect to the root mean square error of the training set (see below) until it changed by <0.01 kJ mol^{-1} or was equal to the number of features, which occurred for the models B and C that use very few features.

In such complex regression problems, there is the danger of using too many fit parameters such that

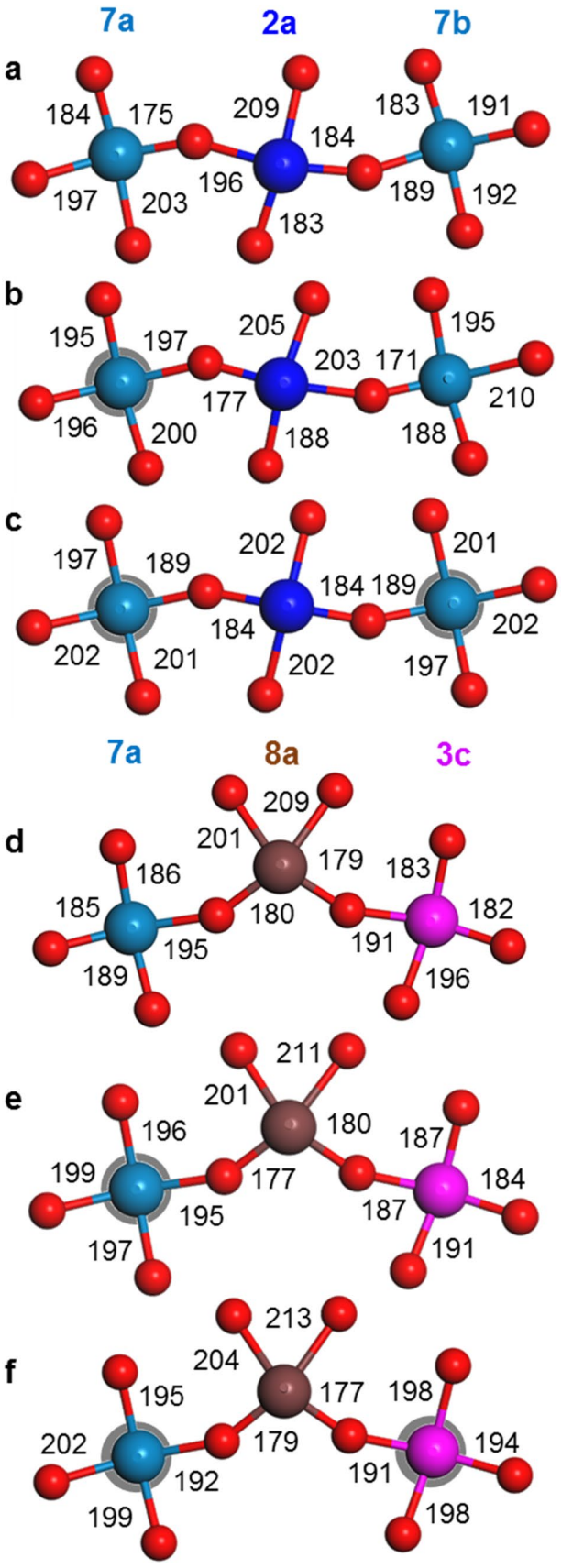

Fig. 2 Equatorial metal-oxygen bond lengths (pm) for two types of V-O-Mo-O-V motifs, around the center **2a**(**Mo**) of a pentameric unit and the center **8a**(**Mo**) in a pentagonal unit, for different states of reduction of the centers **7a**(V), **7b**(V), and **3c**(V). The structures represent the following configurations (**a**) **1 1ab3abcd**, (**b**) and (**e**) **7 1ab3ad7ad**, (**c**) **2 1ab7abcd** and (**d**) **3 1ab3ab7cd**, and (**f**) **10 1ab3ac7ac**; see Table 1. Reduced (polaronic) V centers are marked by a shaded disc in the background: **7a** in panels **b**, **c**, **e**, **f**; **7b** in panel **c**; **3c** in panel **f**

non-generalizable fluctuations in the set of results are replicated in the model; that situation is referred to as "overfitting". One strategy to check for such issues is a cross-validation, based on partitioning all data 75:25 into training and test sets, respectively, where only the first set is used for determining the regression coefficients $\boldsymbol{\varepsilon}$. Subsequently, the quality of the fit is examined by applying the resulting model to the smaller test set. Limitations in the quality of the fitting may be recognized when more complex models do not yield a sufficiently adequate fit for the test set. We report the quality σ_M(set) of prediction as the root mean square error for model M, with "set" referring to the training or test set.

3 Results and discussion

In the current work, we rely on data for 46 symmetry inequivalent structures, beyond the original 14 structures [23], each structure representing a different distribution of small polarons. Recalling the degeneracies of these two sets of structures, we are dealing with 184 and 26 underlying structures, respectively. The additional 46 structures do not exhibit any spatial symmetry; they belong to space group P1. As these structures represent the majority of configurations, it is worthwhile to check how the original linear models [23] B and C carry over to the full universe of 60 polaron distributions—or 210 polaron distributions if degeneracies are accounted for. Next, we will adapt those early models to all structures using the PLSR procedure. Then we continue with model D that analyses the energy characteristics of Mo centers surrounded by polarons. We follow with a discussion of the outliers and their connection to structural aspects. Finally, we will complement these deliberations by discussing aspects of catalytic performance.

3.1 Early linear models B and C for representing a set of DFT energies

For a subset of 14 selected polaron distributions, we earlier presented three models [23] A, B, and C, with

two and three independent variables, respectively, that originally were obtained by a full linear regression, i.e., a least-squares fit:

$$E_A = C_A + \varepsilon_{sh}(1\text{–}3)\, N_{sh}(1\text{–}3) + \varepsilon_{sh}(3\text{–}7)\, N_{sh}(3\text{–}7) \quad (1)$$

$$E_B = C_B + \varepsilon_{sh}\, N_{sh} + \varepsilon_{pp}\, N_{pp} \quad (2)$$

$$E_C = C_C + \varepsilon_{sh}\, N_{sh} + \varepsilon_{pp}\, N_{pp} + \varepsilon_{as2}\, N_{as2} \quad (3)$$

Here, we used the following features of the systems:

(i) the number $N_{sh}(a\text{-}b)$ of (formally) shifted 3*d* electrons from V centers at **1**(V) to **3**(V), $a = 1$ and $b = 3$, or from **3**(V) to **7**(V), $a = 3$ and $b = 7$, taking the structure **1 ≡ 1ab3abcd** as reference [The quantity N_{sh}, without further specification, refers to the total number of shifts, $N_{sh} = N_{sh}(1\text{–}3) + N_{sh}(3\text{–}7)$];
(ii) the number N_{pp} of Mo centers bracketed between two immediately adjacent V^{4+} centers, representing the energy penalty caused by the expanded local V-O equatorial shell, as well as,
(iii) in model C, in addition (*iii*) the number N_{as2} of metal centers **2**(Mo) at the center of the pentameric unit with an asymmetrically reduced/oxidized surrounding along the diagonal **7**(V)–**2**(Mo)–**7**(V).

Thus, the last variable counts the number of pentameric units where exactly one of these centers **7**(V) is oxidized (V^{5+}) and the other one reduced (V^{4+}). All these values N_j are taken per unit cell. Both parameters N_{pp} and N_{as2} characterize the structural flexibility of the metal oxide lattice, probed by the distribution of the (small) polarons. Sometimes we pictorially refer to the metal sites counted by N_{pp} as "squeezed" Mo centers; for examples, see Fig. 2.

As mentioned, the various energy values ε_k were obtained in a least-squares procedure [23], thus quantify the energy contribution of the features just introduced, Table 2. All DFT energies were referenced to the energy of structure **1**. The quantity C_M (M = B, C) represents the intercept at the energy axis of the linear model M. To allow a better comparison with models to be discussed subsequently, Sect. 3.3, we re-evaluated these earlier models using the PLSR procedure in the following subsection.

3.2 Extending models B and C to the full set of 60 structures

To stay comparable with our previous work [23, 24], we kept the previous configuration **1′ 1ab3abcd** as energy reference, although we identified the lower energy isomer **1** in the meantime. This results in the new configuration **1** having a DFT energy of −9.1 kJ mol^{-1} with respect to the previously used reference isomer **1′**. The added 46 configurations span an energy range of 109 kJ mol^{-1}, from −16 kJ mol^{-1} to 93 kJ mol^{-1}. This range is about 80% of the full energy span of 137 kJ mol^{-1} determined for all 60 structures. Hence the 46 configurations do not extend the range of DFT energies at the low or the high end, but rather fill (quite smoothly) gaps between the 14 previous configurations.

As models A and B were fitted to structures **1**–**6**, but were not working well for structures **7**–**14** [23], we expected a rather poor new fit when using the PLSR procedure [40] for the test set of all available polaron distributions, Table S1 of the ESM. This is indeed the case: $\sigma_A(\text{test}) = 19.2$ kJ mol^{-1} and $\sigma_B(\text{test}) = 15.7$ kJ mol^{-1}, Table 2. The reason for this failure was an inadequate description of centers **2** with a single neighboring polaron in the training set. In consequence, a feature N_{aS2} describing these asymmetric centers **2**(Mo) was introduced in model C, Table 2 [23]. The newly fitted PLSR parameters of Model C describe the DFT energies of the 60 structures rather well: $\sigma_C(\text{test}) = 6.1$ kJ mol^{-1}, Table 2, and Fig. 3. Thus, the additional 46 configurations likely do not contain any new feature beyond those already present in the first 14 structures.

Comparing the coefficients of the previous least-squares fits for 6 structures (models A, B), or 14 structures (model C) with the new coefficients from the corresponding PLSR procedures may entail a better understanding of the observed energetics. This comparison should be taken to indicate trends, rather than stringent measures of changes between the two types of least-squares procedures.

We note that especially the energy penalties for polaron shifts increased, by 2.5 kJ mol^{-1} to 12 kJ mol^{-1}. When model A is refit to the larger data set, the parameter $\varepsilon_{sh}(1\text{–}3)$ changes by only 2.5 kJ mol^{-1} to 26.2 kJ mol^{-1}, while $\varepsilon_{sh}(3\text{–}7)$ is modified by 12 kJ mol^{-1} to arrive at 24.0 kJ mol^{-1}. This seems to suggest that treating both shifts differently is not compulsory for the set of 60 structures. Inspecting the common shift coefficient ε_{sh} of models B, and C, one notes that its value increased to 21.6 kJ mol^{-1} and 18.9 kJ mol^{-1}, respectively. The three models A, B, and C produce analogous values within the range of 19–26 kJ mol^{-1} for shifting a polaron.

Going to the full data set, the coefficient ε_{pp} for polaron-polaron interaction increases by 1–2 kJ mol^{-1} for models B and C. Likewise, the energy associated with an asymmetric S2 unit, ε_{aS2} increases by a similar amount, ~2 kJ mol^{-1}, when model C is treated by the PLSR approach, Table 2. These minor modifications underline the generality of model C, as this model is able to represent also the

Table 2 Coefficients (kJ mol^{-1}) and other characteristics of the linear models A, B, C, D and D′ fitting DFT energies[a]

	A[b]	A[c]	B[b]	B[c]	C[b]	C[c]	D[c]	D′[c]
ε_{sh}			14.66	21.58	15.76	18.93		
ε_{sh}(1–3)	23.68	26.18						
ε_{sh}(3–7)	11.70	23.96						
ε_1							−11.97	−17.18
ε_3							6.66	1.44
ε_7							5.31	15.74
ε_{aS2}					−20.08	−18.40		−15.64
ε_{pp}			10.27	12.40	8.15	8.94		
ε_2							46.96	15.69
ε_6							6.30	6.30
ε_8							8.54	8.54
ε_{10}							6.24	6.24
C_M	6.64	−42.72	−40.44	−91.76	−33.11	−47.26	−38.05	−6.78
N_{comp}	–	2	–	2	–	3	6	6
σ_M (train)		17.0		13.1		6.6	8.1	8.1
σ_M (test)		19.2		15.7		6.1	8.7	8.7
R^2 (test)		0.297		0.541		0.933	0.887	0.887
SE (full)	14.4		24.5		7.4			
R^2 (full)	0.910		0.820		0.963			

[a]ε_{sh}—generic energy associated with a polaron shift relative to structure **1**, ε_{sh}(a-b)—energy associated with a polaron shifting from a center *a* to center *b*; ε_1, ε_3, or ε_7—energy contribution per polaron occupying sites **1**(V), **3**(V), and **7**(V); ε_{aS2}—energy associated with the presence of an asymmetric **2**(Mo) center; ε_{pp}—average energy quantifying the polaron-polaron interactions; ε_2, ε_6, ε_8, or ε_{10} —energy associated with a "squeezed" Mo centers at **2**(Mo), **6**(Mo), **8**(Mo), or **10**(Mo); C_M—intercept of model M; N_{comp}—number of components selected in the partial least squares regression (PLSR) procedure; σ_M(set)—root mean square error of the indicated set, train, test, or full (all models previously fitted on the full data set, Ref. [23]); R^2(set)—coefficient of determination of the fit, set = test, full; SE(full)—standard error on the full set as reported in a previous study, Ref. [23]

[b]Previously reported parameters derived from linear regression: model A—6 structures, model B—6 structures, model C—14 structures; Ref. [23]

[c]PLSR applied to the training set, i.e., 45 randomly chosen configurations, including their symmetric congeners, to achieve appropriate weighting, see the ESM

much larger set of polaron distribution energies in a quite reliable way, as indicated by the statistical criteria σ_E(train) = 6.6 kJ mol^{-1}, σ_E(test) = 6.1 kJ mol^{-1}, and R^2(test) = 0.93, Table 2.

When analyzing the outliers of model C, Fig. 3, some common features among them led us to set up linear model E, see Sect. S2 of the ESM. These features, inspired by previous work for MoVNbTeO [42], represent groups of three polarons surrounding two neighboring Mo centers of the pentagonal unit. Yet, the improvement achieved in the description of the energetics is quite small, Table S2 of the ESM.

3.3 Energy model D: an alternative view on features

Next, we will try to improve our understanding of the energetics of various polaron distributions by devising a model with a larger set of features. As just discussed, model C is quite successful in describing the energies of the full set of 60 structures, Table 2. Using one parameter N_{sh} [23] for polaron shifts from sites **1**(V) to **3**(V) as well as from sites **3**(V) to **7**(V) seems plausible also in the light of the PLSR fits of the full set of DFT energies just presented. Yet, it will be worthwhile to examine below this hypothesis in more detail.

However, it seems more questionable to apply a single value for the energy penalty associated with all types of "squeezed" Mo centers **2**(Mo), **6**(Mo), **8**(Mo), and **10**(Mo). In particular, the Mo centers at sites **2**, in the pentameric unit, are stressed by polarons in *trans* locations, while the Mo centers at sites **6**, **8**, and **10**, located in the pentagonal units, undergo "squeezing" by polarons in *cis* locations, Fig. 2. Especially these latter restrictions, rendering model C conceptually rather simple, might miss systematic energy variations.

On the basis of the now available full ensemble of 60 DFT energies, we developed model D, eq. (D), by releasing the restrictions of models B and C:

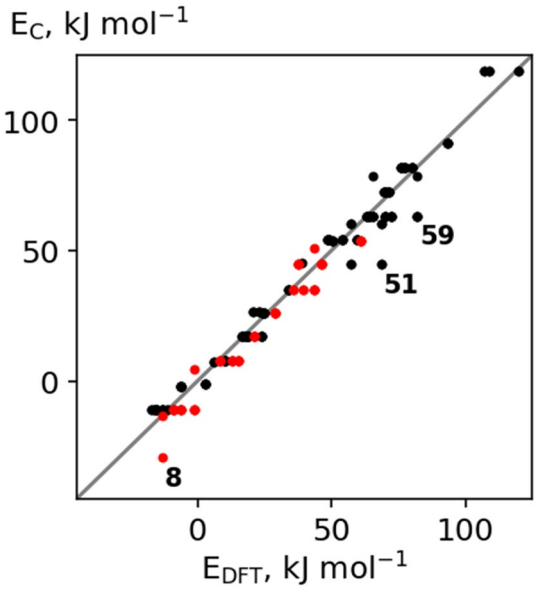

Fig. 3 Comparison of model energies E_C and energies E_{DFT} calculated by a hybrid DFT method. Training set (black) and test set (red) data are shown together with the ideal trend line. Bold numbers (see Table 1) indicate the outliers with deviations of more than 15 kJ mol^{-1}

$$E_D = C_D + \varepsilon_1 N_1 + \varepsilon_3 N_3 + \varepsilon_7 N_7 + \varepsilon_2 N_2 + \varepsilon_6 N_6 + \varepsilon_8 N_8 + \varepsilon_{10} N_{10} \quad (4)$$

Thus, model D has seven features: the numbers N_s of polarons at the sites **1**(V), **3**(V), and **7**(V), as well as the numbers of "stressed" centers at sites **2**(Mo), **6**(Mo), **8**(Mo), and **10**(Mo), Table 2. In all cases, we weighted the structures according to their formal degeneracies. The resulting energy parameters of model D, obtained with six components [39], are shown in Table 2. On the 15 test configurations, model D does not provide a quantitative improvement over model C, $R^2 = 0.885$, $\sigma_D(\text{test}) = 8.7$ kJ mol^{-1}.

However, this latter model was mainly designed for learning more via an alternative set of features whereas the preceding models B and C had been set up to describe energy differences with respect to the energy of a selected reference configuration. Thus, for a more direct numerical comparison to these previous models, we have to resort to differences between energy parameters of model D. To this end, we relate the differences $\varepsilon_3 - \varepsilon_1$ and $\varepsilon_7 - \varepsilon_3$ to the shift value ε_{sh} of, say, model C, Table 2. Indeed, the former difference 18.7 kJ mol^{-1} of model D is almost identical to the value ε_{sh} of model C, 18.9 kJ mol^{-1}.

However, shifting a polaron from site **3**(V) to **7**(V), at, −1.3 kJ mol^{-1} in model D, appears to entail a very different energy change. One may speculate that the relatively low value of ε_7 and the high value of ε_2, Table 2, seem to be connected to the fact that model D is lacking the asymmetric S2 feature of model C. To probe this hypothesis, we added the feature N_{aS2} to model D, generating model D′, Table 2. To a large part, the models D and D′ are of the same quality, with two exceptions. The coefficient $\varepsilon_2 = 15.7$ kJ mol^{-1} is significantly lower, by ~30 kJ mol^{-1}, in model D′, and the difference $\varepsilon_7 - \varepsilon_3 = 14.3$ kJ mol^{-1} is increased by 15.6 kJ mol^{-1}, now of similar size as $\varepsilon_3 - \varepsilon_1 = 18.7$ kJ mol^{-1}. These findings confirm the hypothesis that a compensation is taking place in model D, distributing the favorable (negative!) value ε_{aS2} to the electron shift parameters, $\varepsilon_7 - \varepsilon_3$, lowering it dramatically, while at the same time penalizing the "squeezed" Mo center at S2, ε_2.

We will further illustrate this compensation by moving two polarons from sites **3**(V) to sites **7**(V), adjacent to a center **2a**(Mo). In model C, this would yield

for the first polaron $\varepsilon_{sh} + \varepsilon_{aS2} = 0.5$ kJ mol^{-1}
and the second polaron $2 \cdot \varepsilon_{sh} + \varepsilon_{pp} = 46.8$ kJ mol^{-1},

whereas in model D one generates the energy changes

for the first polaron $\varepsilon_7 - \varepsilon_3 = -1.4$ kJ mol^{-1}
and the second polaron $2 \cdot (\varepsilon_7 - \varepsilon_3) + \varepsilon_2 = 44.3$ kJ mol^{-1}

Thus, on the one hand, the energy consequences in both models are rather similar. On the other hand, models C and D, with their complementary energy decompositions, admit an improved understanding of the various sets of parameters.

Turning to the Mo centers with two neighboring polarons, we notice that our expectation, formulated earlier, was correct, namely the energy $\varepsilon_2 = 47.03$ kJ mol^{-1}, associated with a pentameric unit, is much larger than the coefficients ε_6, ε_8, and ε_{10}, which range from 6.23 kJ mol^{-1} to 8.53 kJ mol^{-1}, Table 2. These latter three energy values are quite comparable to the parameter $\varepsilon_{pp} = 8.93$ kJ mol^{-1} of model C. Thus, two neighboring polarons in *trans* position of a stressed Mo center result in a much larger energy penalty, likely accompanied by other effects.

3.4 Structural aspects

Next, we will inspect the variations in the geometry, triggered by the various polaron distributions. In general, small polarons cause on average a local lattice expansion around a metal center and its equatorial oxygen neighbors. A second effect of such a reduction of V^{5+} to V^{4+} is an adaption of the equatorial oxygen centers such that *trans* located M–O bonds become more similar in lengths. This is related to the pseudo Jahn-Teller concept [43] which states that a d^0 metal center is expected to exhibit

a "non-symmetric" surrounding compared to the corresponding d^1 variant [44]. In consequence, Mo^{6+} centers will usually not be situated close to the center of the rectangle defined by its four equatorial oxygen neighbors, e.g., see center **2a** in Fig. 2a. Locating a polaron on a V center of this material has previously been determined to enlarge the average equatorial bond lengths $\langle(V–O)_{eq}\rangle$ by ~8 pm [23]; this structure change also holds for the 46 newly determined structures of this work, Table S3 of the ESM.

In an exemplary way, we will focus the discussion on the local environments of the centers **2a**(Mo) and **8a**(Mo), i.e., their two neighboring V sites which may be either V^{5+} or V^{4+}, Fig. 2. Center **8a**(Mo) behaves rather comparable to the centers **6a**(Mo) and **10a**(Mo) bracketed by vanadium. Site **2a**(Mo) is located at the center of the so-called pentameric unit [10]. Centers **6a**(Mo), **8a**(Mo), and **10a**(Mo) are part of the pentagonal unit around site **9a**(V) [10], Figure S1 of the ESM. Therefore, one expects them to respond to neighboring polarons in a similar fashion.

To simplify the discussion of these structure motifs, we identify the oxygen center of an equatorial bond by its second neighboring metal center, e.g., **2a**(Mo)–O(**7a**) identifies the bond from **2a**(Mo) to the oxygen center that forms also a bond to **7a**(V), Fig. 2a. There are three scenarios regarding the arrangement of the neighboring polarons: (*i*) no polaron, Figs. 2a, d, (*ii*) one polaron at the neighboring center **7a**(V), Fig. 2b, e, and (*iii*) bracketing polarons at the neighboring V centers, Fig. 2c, f.

(i) Without neighboring polarons, we anticipate a non-symmetric environment in the equatorial Mo–O bonds because of the d^0 situation at the Mo^{6+} centers in question. Indeed, for center **2a**(Mo) the *trans* oriented bonds **2a**(Mo)–O(**7a**) and **2a**(Mo)–O(**7b**) differ by 12 pm, 196 pm vs 184 pm, Fig. 2a. The situation at center **8a**(Mo) is dissimilar, as its *cis* bonds **8a**(Mo)–O(**7a**) and **8a**(Mo)–O(**3c**) differ only by 1 pm, 180 pm vs 179 pm, Fig. 2d. Inspection of the center **7a**(V) in configuration **1** reveals a rather asymmetric center, with differences between *trans* located **7a**(V)–O bonds of more than 19 pm (203 pm – 184 pm), Fig. 2a. The same center **7a**(V) of configuration **3**, although not carrying a polaron, shows only differences of 7–10 pm, Fig. 2d.

(ii) Next, we address the case where center **7a**(V) carries a polaron, V^{4+}. The bond **2a**(Mo)–O(**7a**) is shortened by 19 pm compared to situation (*i*), from 196 pm to 177 pm, Fig. 2b vs Fig. 2a. In turn, the bond **2a**(Mo)–O(**7b**), at the opposite side of the Mo center, elongates by the same amount, from 184 pm to 203 pm. This pattern of alternating bond shortening and elongation progresses to the center **7b**(V), with the 7**b**(V)–O(**2a**) shortened by 18 pm and its trans located bond **7b**(V)–O(**6b**) elongated by 19 pm with respect to situation (*i*). Turning to center **8a**(Mo), we do not observe such strong effects of a polaron located at **7a**(V). The bond **8a**(Mo)–O(**7a**) shortens by 3 pm only, from 180 pm to 177 pm, likely because it was already relatively short, Fig. 2e. We also note a minor effect on the *cis* located bond, **8a**(Mo)–O(**3c**), which expands by 1 pm compared to situation (*i*), 180 pm vs 179 pm, Fig. 2e.

(iii) Finally we inspect the effects when the Mo centers are bracketed by two reduced centers V^{4+}. At center **2a**(Mo), the bond lengths **2a**(Mo)–O(**7a**) and **2a**(Mo)–O(**7b**) are the same, 184 pm. Following the pseudo Jahn-Teller concept in a naïve fashion, this symmetric environment might erroneously lead to assign the Mo center as reduced, Mo^{5+}, d^1 [43]. We notice that also the bonds 7**a**(V)–O(**2a**) and 7**b**(V)–O(**2a**) take the same value, 189 pm. Indeed, also the remaining M–O bonds of centers **7a**(V) and **7b**(V) are very similar, as if the latter site were generated by a point reflection of the former site, Fig. 2c. With polaronic neighbors V^{4+} on either side, also center **8a**(Mo) remains rather symmetric as discussed for situations (*i*) and (*ii*). The bond **8a**(Mo)–O(**7a**) is calculated at 179 pm and the bond **8a**(Mo)–O(**3c**) at 177 pm, Fig. 2f. The bonds, **7a**(V)–O(**8a**) and **3c**(V)–O(**8a**), beyond the adjacent oxygen centers, are also very similar in length, ~191 pm.

Overall, inspecting the position of center **2a**(Mo) within the framework of its equatorial oxygen neighbors, we notice a shift from situation (i), where center **2a**(Mo) is displaced towards center **7b**(V), over situation (ii) where center **2a**(Mo) is shifted towards **7a**(V), to situation (iii) where center **2a**(Mo) is located at the center between both (reduced) V centers. These findings demonstrate how flexibly that center may respond to external influences. These results may even rationalize the high energy penalty when center **2a**(Mo) is "squeezed" by two polarons. Center **8a**(Mo), on the other hand, is located close to centers **7a**(V) and **3c**(V) in all scenarios inspected.

Finally, a remark is in order regarding this structure comparison. We determined alternative isomers of structures **1**, **3,** and **4** that are rather symmetric, see Fig. S2 of the ESM. In all three cases, the equatorial **2a**(Mo)–O bonds in trans position are of the same length, 190 pm in the directions to centers **7**(V) and 193 pm in the directions to centers **4**(Mo). However, in the present discussion, we took into account only the lowest-energy isomers.

3.5 Consequences for catalysis and material design

Structures that feature a single V^{5+} center in the pentameric unit are energetically preferred, which suggests that stable bulk structures contain these motifs. Pentameric units with exactly one V^{5+} center were suggested to be catalytically relevant for the selective oxidation of small hydrocarbons at the M1 phase of MoVNbTeO materials [10]. It was also proposed that (1) a pentameric unit with two V^{4+} centers is not active for the H abstraction reaction from a hydrocarbon, a fundamental step in the subsequent selective partial oxidation, and (2) a pentameric unit with two V^{5+} centers leads to an undesired over-oxidation [10].

For the model unit cell examined in this study, 60 structures of the 210 structures (polaron distributions) in total, feature a single V^{5+} center in both pentameric units. 80 further structures contain one such active site with a single V^{5+} center as well as one pentameric unit with two V^{5+} centers leading to over-oxidation. Twenty four structures exhibit one active and one inactive pentameric unit, i.e., with two V^{4+} centers. In the remaining 46 structures, the pentameric units have no active site, as defined above.

Assuming that for making an impact on the catalyst performance, a structure has to occur at least at 1%. In consequence, configurations up to ~20 kJ mol^{-1} above the ground state should play a role according to the Boltzmann distribution for a reaction temperature of 240 °C. 22 structures that feature a single V^{5+} center in both pentameric units fulfill this condition. This catalytically favorable set represents more than 50% of all structures that would occur at those conditions. Only a single low energy structure (**1**) would not be active at all.

4 Conclusions

We studied the stability trend of V^{4+}/V^{5+} distributions in the bulk structure of the important catalyst material MoVO, using a method based on hybrid density functional theory which admits the localization of unpaired V 3*d* electrons. For this purpose, we selected a (single-layer) unit cell $Mo_{30}V_{10}O_{112}$ motivated by XRD results [7, 11] where the V centers are located at the linker sites **1**(V) and **3**(V), as well as sites **7**(V) of the pentameric unit. Although this is a rather likely scenario, one has to expect variations as the material used in experiment exhibits mixed occupancies [7, 11]. We examined the unit cell of an ideal bulk structure and calculated all 60 unique structures that result from distributing 6 unpaired electrons among the 10 V centers.

We were able to rationalize the (relative) energies by the location of the polaronic quasiparticles, i.e., rather local lattice distortions, as well as consequences of the interactions among these polarons. According to our hybrid DFT modeling, the suggested site crucial in selective oxidation catalysis, namely the pentameric unit with a single V^{5+} center, occurs among the most stable polaron configurations. We developed partial least squares models to correlate the energy variations with the polaron configurations. The energy contribution from polarons and their interaction were related to the position of the polarons as well as their relative location to each other. Further analysis showed that locating polarons at centers **1**(V) is strongly preferred, but "stressed" Mo centers (between two adjacent V^{4+} centers) always lead to less favorable structures. Using linear model D, we elaborated that this energy penalty is especially high for centers **2**(Mo) that may be stressed in *trans* fashion by a pair of polarons at sites **7**(V). Therefore, we expect only low energy configurations when the unpaired electrons are distributed mostly among the V centers at linker sites.

The linear energy models show an increasing complexity. Model A is based on the location of the polarons only, while model B also includes (always unfavorable) polaron-polaron interaction, where two interacting polarons are immediately adjacent to a Mo center. Model C, in addition, features a correction term that characterizes an "asymmetric" site **2** at the center of a pentameric unit; site **2**(Mo) is favorable when it has exactly one polaronic (reduced) V center as neighbor. Finally, we developed model D that offers an alternative energy analysis on the basis of two notions: (*i*) polaron locations, **1**(V), **3**(V), and **7**(V); (*ii*) the stressed Mo centers with two adjacent V polaron centers, namely **2**(Mo), **6**(Mo), **8**(Mo), **10**(Mo). In consequence, we arrived at the coefficients of our explanatory model D with the energy ordering of the polaron locations as $\mathbf{1} < \mathbf{3} \approx \mathbf{7}$, and noted that stressing **2**(Mo) by two neighboring polarons is particularly costly in energy.

Acknowledgements We gratefully acknowledge stimulating discussions with Juan Arce-Ramos and Adrian Hühn. This work was supported by grant no. 1527700033 of the A*STAR Science and Engineering Research Council. Furthermore, this work profited from generous allotments of computational resources at the National Supercomputing Center Singapore and the A*STAR Computational Resource Center.

Authors' contributions T.F. and W.L. calculated the structures, designed model D, and wrote the initial draft of the manuscript. A.G. designed the project, supervised the research, revised the statistical models as well as the manuscript. N.R. designed the project, supervised the research, and revised the manuscript.

Funding This work was supported by grant no. 1527700033 of the A*STAR Science and Engineering Research Council.

Availability of data and materials As Electronic Supplementary Material (ESM), we provide (*i*) additional details on the statistical procedure, (*ii*) figures illustrating the distributions of reduced vanadium

centers, (*iii*) model E for the analysis of outliers of model C, and (*iv*) an archive of atomic coordinates of optimized structures in cif format.

Code availability As referenced and described in detail, we applied commercial codes or codes freely available.

Compliance with ethical standards

Conflict of interest The authors declare that they have no conflict of interest.

References

1. Ivars F, López Nieto JM (2014) In: Duprez D, Cavani F (eds) Handbook of advanced methods and processes in oxidation catalysis. From laboratory to industry. World Scientific Press, Singapore, pp 767–834
2. C-c C, Vogt T, Zhao L-L, Genest A, Rösch N (2015) Structure and electronic properties of MoVO type mixed-metal oxides—a combined view by experiment and theory. Dalton Trans 44(31):13778–13795. https://doi.org/10.1039/c5dt01694k
3. Watanabe N, Ueda W (2006) Comparative study on the catalytic performance of single-phase Mo–V–O-based metal oxide catalysts in propane ammoxidation to acrylonitrile. Ind Eng Chem Res 45(2):607–614. https://doi.org/10.1021/ie0509286
4. Chen C, Kosuke N, Murayama T, Ueda W (2013) Single-crystalline-phase Mo_3VO_x: an efficient catalyst for the partial oxidation of acrolein to acrylic acid. ChemCatChem 5:2869–2873. https://doi.org/10.1002/cctc.201300268
5. Katou T, Vitry D, Ueda W (2003) Hydrothermal synthesis of a new Mo–V–O complex metal oxide and its catalytic activity for the oxidation of propane. Chem Lett 32:1028–1029. https://doi.org/10.1246/cl.2003.1028
6. Ishikawa S, Yi X, Murayama T, Ueda W (2014) Catalysis field in orthorhombic Mo_3VO_x oxide catalyst for the selective oxidation of ethane, propane and acrolein. Catal Today 238:35–40. https://doi.org/10.1016/j.cattod.2013.12.054
7. Ishikawa S, Kobayashi D, Konya T, Ohmura S, Murayama T, Yasuda N, Sadakane M, Ueda W (2015) Redox treatment of orthorhombic $Mo_{29}V_{11}O_{112}$ and relationships between crystal structure, microporosity and catalytic performance for selective oxidation of ethane. J Phys Chem C 119(13):7195–7206. https://doi.org/10.1021/jp512848w
8. Murayama H, Vitry D, Ueda W, Fuchs G, Anne M, Dubois JL (2007) Structure characterization of orthorhombic phase in MoVTeNbO catalyst by powder X-ray diffraction and XANES. Appl Catal A: Gen 318:137–142. https://doi.org/10.1016/j.apcata.2006.10.050
9. Li X, Buttrey DJ, Blom DA, Vogt T (2011) Improvement of the structural model for the M1 phase Mo–V–Nb–Te–O propane (amm)oxidation catalyst. Top Catal 54(10–12):614–626. https://doi.org/10.1007/s11244-011-9684-z
10. Grasselli RK, Volpe AF (2014) Catalytic consequences of a revised distribution of key elements at the active centers of the M1 phase of the $MoVNbTeO_x$ system. Top Catal 57(14–16):1124–1137. https://doi.org/10.1007/s11244-014-0286-4
11. Lunkenbein T, Girgsdies F, Wernbacher A, Noack J, Auffermann G, Yasuhara A, Klein-Hoffmann A, Ueda W, Eichelbaum M, Trunschke A et al (2015) Direct imaging of octahedral distortion in a complex molybdenum vanadium mixed oxide. Angew Chem Int Ed 54(23):6828–6831
12. Rozanska X, Fortrie R, Sauer J (2007) Oxidative dehydrogenation of propane by monomeric vanadium oxide sites on silica support. J Phys Chem C 111(16):6041–6050. https://doi.org/10.1021/jp071409e
13. Rozanska X, Sauer J (2009) Oxidative dehydrogenation of hydrocarbons by $V_3O_7^+$ compared to other vanadium oxide species. J Phys Chem A 113(43):11586–11594. https://doi.org/10.1021/jp9005235
14. Fu G, Xu X, Sautet P (2012) Vanadium distribution in four component MoVTeNb mixed oxide catalysts from first principles: how to explore the numerous configurations? Angew Chem 124(51):12800–12800. https://doi.org/10.1002/ange.201207638
15. Getsoian AB, Bell AT (2013) The influence of functionals on density functional theory calculations of the properties of reducible transition metal oxide catalysts. J Phys Chem C 117(48):25562–25578. https://doi.org/10.1021/jp409479h
16. Yu J, Xu Y, Guliants VV (2014) Propane ammoxidation over Mo–V–Te–Nb–O M1 phase investigated by DFT: Elementary steps of ammonia adsorption, activation and NH insertion into π-allyl intermediate. Top Catal 57(14-16):1145–1151. https://doi.org/10.1007/s11244-014-0280-x
17. Fjermestad T, Li W-Q, Rugg G, Ishida S, Okuno M, Sagi K, Genest A, Rösch N (2018) Acrolein oxidation to acrylic acid over the $MoVO_x$ material. Insights from DFT modeling. Appl Catal A: Gen 565:68–75. https://doi.org/10.1016/j.apcata.2018.07.044
18. Shiju NR, Rondinone AJ, Mullins DR, Schwartz V, Overbury SH, Guliants VV (2008) XANES study of hydrothermal Mo–V-based mixed oxide M1-phase catalysts for the (amm)oxidation of propane. Chem Mater 20(21):6611–6616. https://doi.org/10.1021/cm800546h
19. Shiju NR, Guliants VV, Overbury SH, Rondinone AJ (2008) Toward environmentally benign oxidations: bulk mixed MoV(TeNb)O M1 phase catalysts for the selective ammoxidation of propane. ChemSusChem 1(6):519–523. https://doi.org/10.1002/cssc.200800039
20. Trunschke A, Noack J, Trojanov S, Girgsdies F, Lunkenbein T, Pfeifer V, Hävecker M, Kube P, Sprung C, Rosowski F (2017) The impact of the bulk structure on surface dynamics of complex Mo–V-based oxide catalysts. ACS Catal 7(4):3061–3071. https://doi.org/10.1021/acscatal.7b00130
21. Andrushkevich TV (1993) Heterogeneous catalytic oxidation of acrolein to acrylic acid: mechanism and catalysts. Catal Rev-Sci Eng 35:213–259. https://doi.org/10.1080/01614949308014606
22. Heine C, Hävecker M, Sanchez-Sanchez M, Trunschke A, Schlögl R, Eichelbaum M (2013) Work function, band bending, and microwave conductivity studies on the selective alkane oxidation catalyst MoVTeNb oxide (orthorhombic M1 phase) under operation conditions. J Phys Chem C 117(51):26988–26997. https://doi.org/10.1021/jp409601h
23. Li W-Q, Fjermestad T, Genest A, Rösch N (2018) How the distribution of reduced vanadium centers affects structure and stability of the $MoVO_x$ material. Catal Sci Technol 8:2654–2660. https://doi.org/10.1039/c8cy00402a
24. Li W-Q, Fjermestad T, Genest A, Rösch N (2019) Reactivity trends of the $MoVO_x$ mixed metal oxide catalyst from density functional modeling. Catal Sci Technol 9(7):1559–1569. https://doi.org/10.1039/C8CY02545B
25. Maxisch T, Zhou F, Ceder G (2006) Ab initio study of the migration of small polarons in olivine Li_xFePO_4 and their association with lithium ions and vacancies. Phys Rev B 73(10):104301. https://doi.org/10.1103/PhysRevB.73.104301
26. Chrétien S, Metiu H (2011) Electronic structure of partially reduced rutile TiO_2(110) surface: where are the unpaired electrons located? J Phys Chem C 115(11):4696–4705. https://doi.org/10.1021/jp111209a

27. Becke AD (1993) Density-functional thermochemistry. III. The role of exact exchange. J Chem Phys 98:5648–5652. https://doi.org/10.1007/s002149900065
28. Dovesi R, Orlando R, Erba A, Zicovich-Wilson CM, Civalleri B, Casassa S, Maschio L, Ferrabone M, De La Pierre M, D'Arco P (2014) CRYSTAL14: a program for the ab initio investigation of crystalline solids. Int J Quantum Chem 114(19):1287–1317. https://doi.org/10.1002/qua.24658
29. Dinda S, C-c C, Genest A, Rösch N (2016) Evaluation of density functionals for elementary steps of selective oxidation reactions. Comput Theor Chem 1101:36–45. https://doi.org/10.1016/j.comptc.2016.12.021
30. Rugg G, Genest A, Rösch N (2018) DFT variants for mixed-metal oxides. Benchmarks using multi-center cluster models. J Phys Chem A 122(35):7042–7050. https://doi.org/10.1021/acs.jpca.8b05331
31. Grimme S (2006) Semiempirical GGA-type density functional constructed with a long-range dispersion correction. J Comput Chem 27:1787–1799. https://doi.org/10.1002/jcc.20495
32. Ruiz E, Llunell M, Alemany P (2003) Calculation of exchange coupling constants in solid state transition metal compounds using localized atomic orbital basis sets. J Solid State Chem 176(2):400–411. https://doi.org/10.1016/S0022-4596(03)00238-X
33. Bredow T, Jug K, Evarestov RA (2006) Electronic and magnetic structure of $ScMnO_3$. Phys Status Solidi 243(2):R10–R12. https://doi.org/10.1002/pssb.200541403
34. Dovesi R, Ermondi C, Ferrero E, Pisani C, Roetti C (1984) Hartree-Fock study of lithium hydride with the use of a polarizable basis set. Phys Rev B 29(6):3591. https://doi.org/10.1103/PhysRevB.29.3591
35. Cora F, Patel A, Harrison NM, Roetti C, Richard A, Catlow C (1997) An ab initio Hartree-Fock study of α-MoO_3. J Mater Chem 7(6):959–967. https://doi.org/10.1039/a607439a
36. Hay PJ, Wadt WR (1985) Ab initio effective core potentials for molecular calculations. Potentials for K to Au including the outermost core orbitals. J Chem Phys 82:299–310. https://doi.org/10.1063/1.448975
37. Monkhorst HJ, Pack JD (1976) Special points for brillouin-zone integrations. Phys Rev B 13(12):5188. https://doi.org/10.1103/PhysRevB.13.5188
38. Dovesi R, Saunders VR, Roetti C, Orlando R, Zicovich-Wilson CM, Pascale F, Civalleri B, Doll K, Harrison NM, Bush IJ, D'Arco P, Llunell M, Causà M, Noël Y (2014) CRYSTAL14 User's manual. University of Torino, Torino, Italy
39. Haenlein M, Kaplan AM (2004) A beginner's guide to partial least squares analysis. Understand Statist 3(4):283–297. https://doi.org/10.1207/s15328031us0304_4
40. Pedregosa F, Varoquaux G, Gramfort A, Michel V, Thirion B, Grisel O, Blondel M, Prettenhofer P, Weiss R, Dubourg V (2011) Scikit-learn: machine learning in Python. J Mach Learn Res 12(Oct):2825–2830
41. Wold S, Sjöström M, Eriksson L (2001) PLS-regression: a basic tool of chemometrics. Chemom Intell Lab Syst 58(2):109–130. https://doi.org/10.1016/S0169-7439(01)00155-1
42. Arce-Ramos JM, Genest A, Rösch N (2020) How TeO defects in the MoVNbTeO catalyst material affect the V^{4+} distribution. A computational study. J Phys Chem C 124(34):18628–18638. https://doi.org/10.1021/acs.jpcc.0c05447
43. Bersuker IB (2013) Pseudo-Jahn–Teller effect—a two-state paradigm in formation, deformation, and transformation of molecular systems and solids. Chem Rev 113(3):1351–1390. https://doi.org/10.1021/cr300279n
44. Kunz M, Brown ID (1995) Out-of-center distortions around octahedrally coordinated d^0 transition metals. J Solid State Chem 115:395–406. https://doi.org/10.1006/jssc.1995.1150